Chinese Journal of
POLYMER SCIENCE

RESEARCH ARTICLE

https://doi.org/10.1007/s10118-024-3119-3
Chinese J. Polym. Sci. **2024**, *42*, 851–863

The Effect of Blending Ratio on the Structure and Properties of the PPR/PS *In situ* Fiber Reinforced System Prepared by Multi-Flow Vibration Injection Molding

Yan-Jiang Li, Meng-Long Hu, Jun-Wen Zhang, Qiang Fu, and Jie Zhang*

College of Polymer Science and Engineering, State Key Laboratory of Polymer Materials Engineering, Sichuan University, Chengdu 610065, China

Abstract To enhance the mechanical properties of polypropylene random copolymer (PPR), polystyrene (PS) with four different contents were added to the PPR matrix through melt blending. Subsequently, using the Multi-Flow Vibration Injection Molding (MFVIM) technology, PPR/PS *in situ* microfiber composites (MFC) with different blending ratios were prepared. The results indicated that blending ratio had a great impact on the phase morphology and crystal structure of MFVIM samples, which was different from those of conventional injection molding (CIM) samples. PS ultrafine fibers could be formed under the shear field and could absorb the PPR molecular chains to form hybrid shish-kebab structures. Meanwhile, the PPR matrix could also form shish-kebab structures under the effect of strong shear. When the PS content reached 20%, under the combined action of PS *in situ* microfibers and highly oriented crystal structure, the tensile strength and Young's modulus of the sample were obviously improved and the impact strength remained at a relatively high level. So a strong and tough balanced PPR based material was obtained. These results provide valuable insights for expanding the industrial and daily-life applications of PPR and show promising development prospects.

Keywords PPR; MFVIM; *In situ* microfibers; Shear field; Hybrid shish-kebab structures

Citation: Li, Y. J.; Hu, M. L.; Zhang, J. W.; Fu, Q.; Zhang, J. The effect of blending ratio on the structure and properties of the PPR/PS *in situ* fiber reinforced system prepared by multi-flow vibration injection molding. *Chinese J. Polym. Sci.* **2024**, *42*, 851–863.

INTRODUCTION

Compared with small molecule materials, the molecular chain structure of polymers is complex and has obvious viscoelasticity, so it provides the possibility to regulate the aggregation structure through processing methods, which are the key factors affecting their final performance.[1–3] Studies have shown that some new processing technologies such as shear-controlled orientation injection molding (SCORIM),[4] dynamic packing injection molding (DPIM),[5] loop oscillatory push-pull molding (LOPPM),[6] multi-flow vibration injection molding (MFVIM)[7] can provide strong shear action and introduce plenty of oriented structures into the polymers, significantly improving their strength, modulus, and hardness.[8,9] Kalay[4] used SCORIM device to process isotactic polypropylene (*i*PP) products, the results demonstrated that the Young's modulus and tensile strength were increased by 80% and 65%, respectively. Liang *et al.*[5] fabricated the LLDPE/HDPE samples using DPIM and observed highly oriented shish-kebab structures throughout the thickness direction of the samples, so the tensile strength was increased by more than 40%. Liu *et al.*[6] studied the synergistic enhancement effect of UHMWPE on HDPE under oscillatory shear field and found that the tensile strength, Young's modulus and toughness of the products were respectively increased by 2.8, 4.9 and 5.8 times, even better than many common engineering plastics. Huang *et al.*[10] utilized the pre-shear injection molding device to process HDPE and discovered that the tensile strength was increased from 24.8 MPa to 32.8 MPa. Hong *et al.*[7] used MFVIM technology to process UHMWPE/HDPE samples and got that the tensile strength and modulus were increased to 2.14 and 1.39 times, respectively. Mi *et al.*[11] prepared fully oriented *i*PP samples containing a large number of shish-kebab structures by combining MFVIM technology and melting-recrystallization process, the results indicated that the impact strength of the sample increased by 158%. However, in all of the above studies, the materials selected are of highly crystalline materials (such as HDPE, *i*PP), while almost no research concerns materials with low crystallinity. The reason may be that the molecular chains of highly crystalline materials are more regular and easier to move, which makes the effect of shear more obvious to promote crystallization process and also leads to a greater improvement in mechanical properties.

In addition to using processing methods to improve polymer mechanical performance, adding fibers is also a common way to reinforce the matrix material.[12,13] Nevertheless, the compatibility of the blend and the issue of fiber distribution need to be considered.[14] Recently, *in situ* microfiber composites (MFC) have attracted researchers' interest due to

* Corresponding author, E-mail: zhangjie@scu.edu.cn

Received January 3, 2024; Accepted March 6, 2024; Published online April 8, 2024

their enormous potential in functionalization and mechanical reinforcement.[15–17] Compared with conventional inorganic fibers, polymeric fibers prepared *in situ* have higher flexibility and aspect ratio, which can greatly strengthen the mechanical properties of materials.[18,19] MFC can be prepared by stretching or shearing dispersed particles in the matrix into microfibers or nanofibers through different processing methods. The traditional preparation process can be generally divided into three steps: (1) melt blending: extruding two incompatible polymers with significant differences in melting points, (2) fibrillating: stretching the extruded material to make the dispersed phase deform into fibers, (3) subsequent processing: using a certain processing method to restore the isotropy of the matrix phase, while preserving the fiber structure formed by the dispersed phase.[20,21] However, the subsequent processing process may change the interfacial condition between the matrix and microfibers, and can cause the formed fibers to aggregate and break, thereby affecting the final performance of the materials.[22] Fortunately, with the continuous development of processing technology, research on the combination of *in situ* fiber forming and various advanced processing methods has also made significant progress, which can make the dispersed phase form *in situ* fibers directly during processing. Zhou *et al*.[23,24] conducted systematic research on improving the mechanical properties of PP/LDPE blend systems, they used CIM with a foaming technology to fabricate super-ductile PP/LDPE samples and then stretched the samples to form *in situ* cold-drawn fiber (CDF). The results demonstrated that the CDFs had an excellent reinforcement effect and the strain-at-break could be as high as 650% before the sample fracture. Kelnar *et al*.[25] combined *in situ* fiber forming with micro injection molding (MIM) to prepare HDPE/PA6 MFC, the mechanical test results indicated that the Young's modulus and impact strength of the samples were improved and the optimal impact toughness could reach 29 kJ/m^2. Dadouche *et al*.[26] used blow molding technology to prepare PBSA/PA11 MFC based on all organisms. The diameter of PA11 microfibers could be as low as 300 nm, and the results exhibited that the elongation at break and impact toughness of the samples were increased by four and five times, respectively. Jiang *et al*.[27] prepared PP/PS MFC by Fused Filament Fabrication (FFF) and found the tensile strength was increased by 42.6%, and the impact strength could reach 55.96 kJ/m^2. Xia *et al*.[28] utilized Gas Assisted Injection Molding (GAIM) technology to prepare HDPE/PC MFC. Compared with conventional injection molding (CIM) samples, the yield strength of samples prepared by GAIM increased by 66%. Jiang *et al*.[29] prepared HDPE/PS MFC by using MFVIM, the results showed that the sample with 20% PS added had the highest tensile strength (40 MPa) and relatively high impact strength.

Polypropylene (PP) is a widely used general plastic with excellent performance and low cost since its first commercial production in 1957, thanks to the continuous improvement of catalyst technology and production processes.[30–32] With the development of the polymer industry, PP can be classified into three categories based on the presence and distribution of ethylene monomers in the polymer chain: polypropylene homopolymer(PPH), polypropylene block copolymer (PPB), and polypropylene random copolymer (PPR).[33,34] For PPR, ethylene monomers are randomly distributed within the polymer chain, which disrupts the regularity and leads to a decrease in crystallinity and melting point.[35,36] Thus PPR exhibits excellent impact resistance and is extensively used in applications such as pipes, automobile parts, furniture, and packaging.[37–39] Compared to PPH, PPR has significantly improved impact toughness but lower strength and stiffness.[40] Therefore, improving the mechanical strength of PPR while ensuring its relatively high impact toughness is of great theoretical and practical research significance.

In this work, we choose PPR and PS to prepare MFC by using MFVIM technology, while exploring the impact of blending ratio on the structure and performance of this blend system. It is expected that the PS phase can form *in situ* fibers and improve the crystallization ability of the PPR matrix through heterogeneous nucleation. At the same time, we also hope that shish-kebab structures can be formed in the PPR matrix under the shear action. Herein, we analyzed the morphology and crystal stucture of the system using scanning electron microscopy (SEM), differential scanning calorimetry (DSC), small angle X-ray scattering (SAXS). The results indicate that the blending ratio has a far-reaching effect on the microfiber morphology, crystallization behavior, and ultimately mechanical properties of the blend system. Simultaneously, under the combined effect of *in situ* fibers and oriented structures, the strength and modulus of the sample with 20% PS content are significantly improved, while the impact toughness remains at a high level. Therefore, a strong and tough balanced PPR based material is successfully obtained.

EXPERIMENTAL

Material

Polypropylene random copolymer (PPR, brand R200P) was purchased from South Korean Hyosung company. Its melt flow rate (MFR) is 0.25 g/10min (230 °C, 2.16 kg), and its weight average molecular weight M_w is 7.2×10^5 g/mol, with an ethylene monomer content of 3.8%. Polystyrene (PS, brand PS5250) was purchased from Taihua Petrochemical, with a MFR of 7 g/10min (200 °C, 5 kg).

Sample Preparation

Firstly, PPR and PS pellets were dried at 80 °C for 8 h to remove moisture. In this experiment, four different PPR / PS blending ratios were designed, in which the mass fractions of PS were 5 wt%, 10 wt%, 20 wt% and 30 wt%, respectively. Then, PPR/PS pellets with different blending ratios were fully melted and mixed by a SHJ-25 corotating twin-screw extruder (Nanjing Chengmeng Plastic Machinery Factory). The temperatures from hopper to die were set to 80, 100, 130, 160, 180, 200, 200 and 180 °C in sequence, the feeding screw speed was 20 r/min and the host screw speed was 200 r/min. Next, the extruded melt was pulled into filaments and cooled by a cold water tank before granulation. The obtained PPR/PS blend pellets were dried at 80 °C for 12 h for the next experimental use.

The self-made MFVIM equipment[7,8] was used for injection

molding of fully dried PPR/PS blend pellets. The mold used has an overflow at the end of the cavity. During the packing stage, the injection piston can push the melt into the overflow under the action of the vibration pressure, forming multiple melt flows. Therefore, the melt will experience strong shear effects during the forming process. The temperatures of each section from hopper to die were 160, 180, 210 and 230 °C, respectively. The mold temperature was 40 °C. By adjusting the process parameters of MFVIM, including vibration pressure, vibration frequency, and vibration interval time, the final structure of the injection molded sample could be controlled. The schematic diagram of the relationship between vibration pressure and time during the packing stage is shown in Fig. 1, and the relevant process parameters are shown in Table 1. The duration time of each vibration is 0.5 s. For comparison purposes, corresponding conventional injection molding (CIM) samples were also prepared, including neat PPR and PPR/PS samples with different blending ratios. The processing parameters of CIM samples were consistent with those of MFVIM samples, except that the packing pressure remained constant at P_0 (48 MPa). The samples were named based on the PS content and preparation method. For example, C-5PS refers to PPR/PS samples with a PS mass fraction of 5 wt% formed by CIM, and V-10PS refers to PPR/PS samples with a PS mass fraction of 10 wt% formed by MFVIM. The sampling schematic diagram of various characterization methods is shown in Fig. 2.

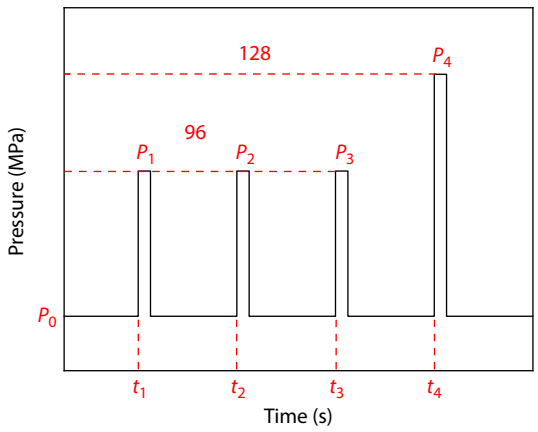

Fig. 1 Schematic diagram of the relationship between vibration pressure and time during packing stage.

Characterizations

Thermogravimetric analysis (TGA)

The thermal stability of materials was measured by a thermal gravimetric analyzer (NETZSCH, TG209F1). The mass of each sample was 3–8 mg and the test was conducted in a nitrogen atmosphere with a flow rate of 60 mL/min. The temperature was increased from 35 °C to 800 °C at a heating rate of 10 °C/min.

Rheological performance testing

The relationship between apparent viscosity and shear rate of PPR and PS was studied using a RH7D high-pressure capillary rheometer (Malvern Instruments, UK). The diameter of the capillary die was 1 mm, and the aspect ratio was 20:1. After the material stayed in the cylinder for 3 min, it was extruded at a constant temperature of 230 °C, and the range of shear rate was from 1 s^{-1} to 5000 s^{-1}.

Differential scanning calorimetry (DSC)

The melting and crystallization behavior of all samples was tested using a TA Q200 differential scanning calorimeter (TA, USA). Each sample about 3–8 mg was placed in an aluminum crucible and all measurements were conducted under a dry nitrogen atmosphere. In order to know the crystallization of PPR matrix under the action of shear field, the samples were first heated from 40 °C to 200 °C at a heating rate of 10 °C/min and the results were recorded. After eliminating the thermal and mechanical history at 200 °C for 5 min, the samples were then cooled from 200 °C to 40 °C at a cooling rate of 10 °C/min and were heated once again from 40 °C to 200 °C at the same heating rate to get more information about the non-isothermal crystallization behavior of the blends. Furthermore, the samples were cooled from 200 °C to 122 °C at a cooling rate of 40 °C/min for isothermal crystallization. The crystallinity X_c of the samples was calculated according to the following equation:

$$X_c = \frac{\Delta H_m}{w_f \Delta H_m^0} \times 100\% \quad (1)$$

where ΔH_m represents the melting enthalpy of PPR during the heating process, ΔH_m^0 represents the absolute crystallization enthalpy of PP, which is 207 J/g,[41] w_f represents the mass fraction of PPR in the blend.

Scanning electron microscopy (SEM)

To observe the phase morphology along the melt flow direction, the PS phase was etched away by xylene for 2 h at 20 °C and then the etched surface was cleaned with distilled water in an ultrasonic cleaner. To further display the interior crystalline morphology, the samples were further etched in an acid solution for 8 h at 60 °C. The solution contained sulfuric acid, phosphoric acid, and distilled water in a volume ratio of 10:4:1. After gold sputtering treatment, the etched surfaces were observed using a field-emission scanning electron microscope (Inspect F, FEI, Nova Nano SEM450) with an accelerating voltage of 10 kV.

Small angle X-ray scattering (SAXS)

The samples were tested using a small angle X-ray scattering instrument system (Xeuss 2.0) from Xenocs company in France. The detector (Pilatus 300K) used for testing was produced by Detris company in Switzerland. The light source was a copper target with a wavelength of 0.154 nm and the exposure time was 180 s.

Table 1 Processing parameters during packing stage.*

	Injection/Packing pressure P_0	First		Second		Third		Fourth	
		P_1	t_1	P_2	t_2	P_3	t_3	P_4	t_4
CIM	48	–	–	–	–	–	–	–	–
VIM		96	1	96	5	96	9	128	13

*P: pressure (MPa) and t: start time (s)

https://doi.org/10.1007/s10118-024-3119-3

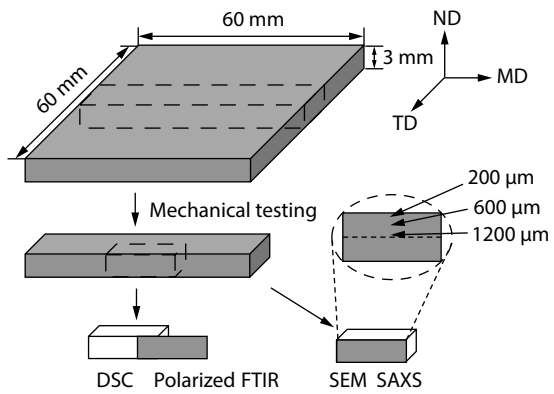

Fig. 2 The schematic diagram of sampling methods for the characterizations. MD, ND and TD are the melt flow direction, the normal direction and the transverse direction, respectively.

Polarized Fourier transform infrared spectroscopy (polarized FTIR)

By adding a polarizer to the optical path of a Nicolet-IS10 (Thermo Electron Co., USA) infrared spectrometer, polarized infrared spectra could be obtained. When the electric vector direction of the polarized light was parallel and perpendicular to the material orientation direction, the absorbance of the spectral bands of different directions ($A_{\parallel}$ and $A_{\perp}$) were measured, respectively. Orientation function f and absorbance A has the following relationship:[42]

$$f = [(R-1)/(R+2)]/[(3\cos^2\alpha - 1)/2] \quad (2)$$

$$R = A_{\parallel}/A_{\perp} \quad (3)$$

where R is the dichroism ratio, α is the angle between the dipole moment vector and the molecular chain, and the value is 18°.[43]

Mechanical testing

The samples were cut into standard dumbbell bars for the tensile strength test, which was measured by an electronic universal testing machine (Instron 5569) with a 50 mm/min cross-head speed at room temperature. Standard rectangular bars were made for the notch Izod impact strength test performed by a VJ-40 Izod machine at room temperature. Before the test, a 45° V-shaped notch with a depth of 2 mm was milled in the middle position of the sample. The values of the mechanical properties were obtained by taking the average of at least five samples.

RESULTS AND DISCUSSION

Thermal Stability

The TGA and differential thermogravimetric analysis (DTG) curves of PPR, PS and their blends are shown in Fig. 3. For PS, the initial degradation temperature ($T_{2\%}$) is 318.1 °C and the maximal degradation rate appears at 372.3 °C. The $T_{2\%}$ of neat PPR is 399.2 °C and the temperature corresponding the maximum degradation rate is 456.2 °C, which is 83.9 °C higher than PS. The complete degradation temperatures of PS and PPR are 400 and 480 °C, respectively. These results indicate that the thermal stability of PS is not as good as PPR. The thermal stability of the blends is between pure PPR and PS, and tends to be closer to PPR, which means PPR plays a dominant role as the matrix. Besides, with the PS content in the blend increases, the thermal stability also decreases.

Rheological Behavior

The capillary rheological curves of PPR and PS are shown in Fig. 4(a). Within the shear rate range of 1–5000 s^{-1}, the apparent viscosity of PPR and PS decreases with the increase of shear rate, exhibiting a typical shear thinning behavior. This is because the increase in shear rate leads to an increase of molecular chain orientation and a decrease of molecular chain entanglement density. Compared with PPR, PS has a lower viscosity throughout the entire shear rate range.

Generally speaking, the viscosity ratio of the dispersed phase to matrix phase (η_d/η_m) in the blend have a prominent impact on the final morphology and structure of materials.[44–47] Their results indicates that when η_d/η_m is less than 1, it is beneficial for the deformation of the dispersed phase and the maintenance of the microfiber structure. When η_d/η_m is greater than 1.5, the adhesion forces of the matrix are too weak to maintain the fibrous deformation state of the dispersed phase. The variation of viscosity ratio between PS and PPR within the shear rate range is shown in Fig. 4(b). It is found that the η_{PS}/η_{PPR} is less than 0.7, so it is possible for PS phase to form *in situ* fibers and maintain fiber morphology after experiencing strong shear field during MFVIM processing.

Crystallization Behavior

Figs. 5(a) and 5(b) respectively show the first melting curves of CIM and MFVIM samples, which can intuitively reflect the influence of external field on the crystallization behavior of the

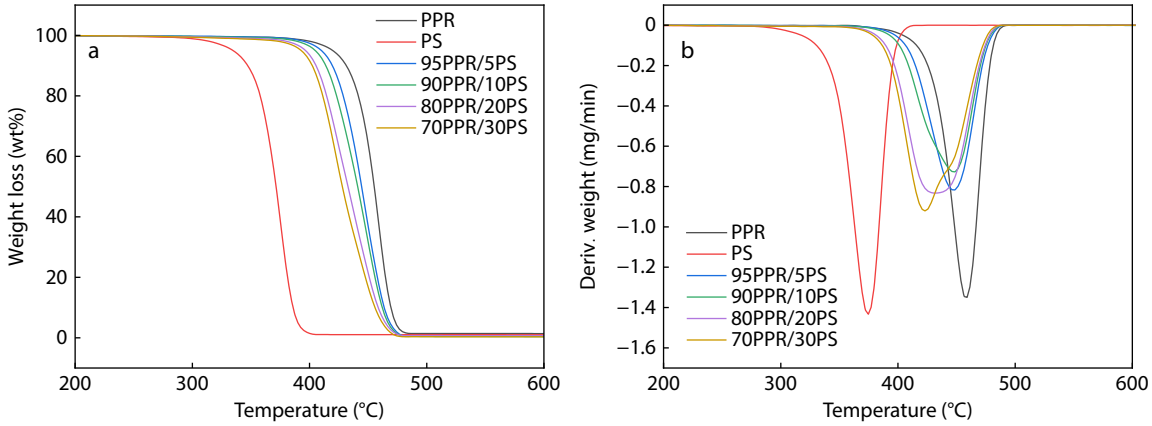

Fig. 3 TGA curves (a) and DTG curves (b) of PPR, PS, and their blends with different blending ratio.

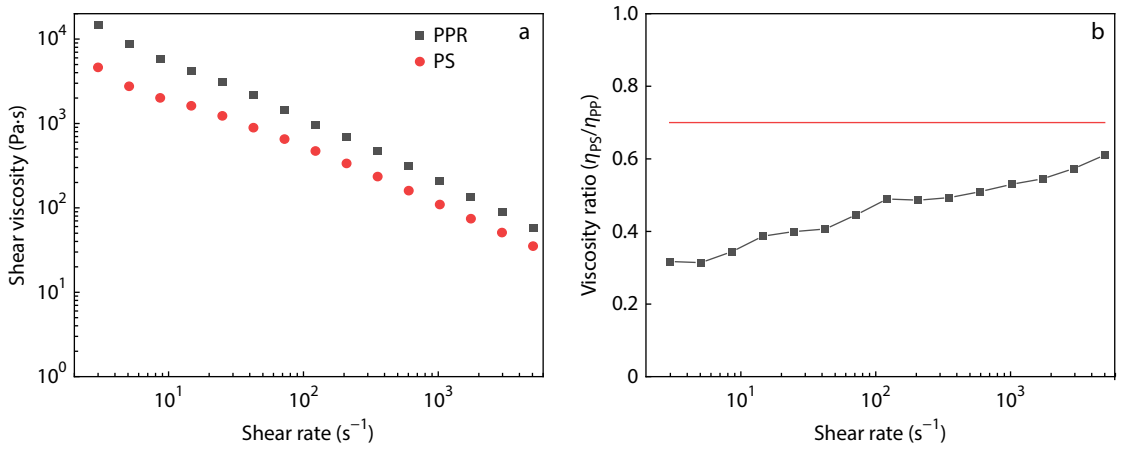

Fig. 4 The rheological results of PPR and PS: (a) the shear viscosity and (b) the viscosity ratio of η_{PS}/η_{PPR} changes with shear rate.

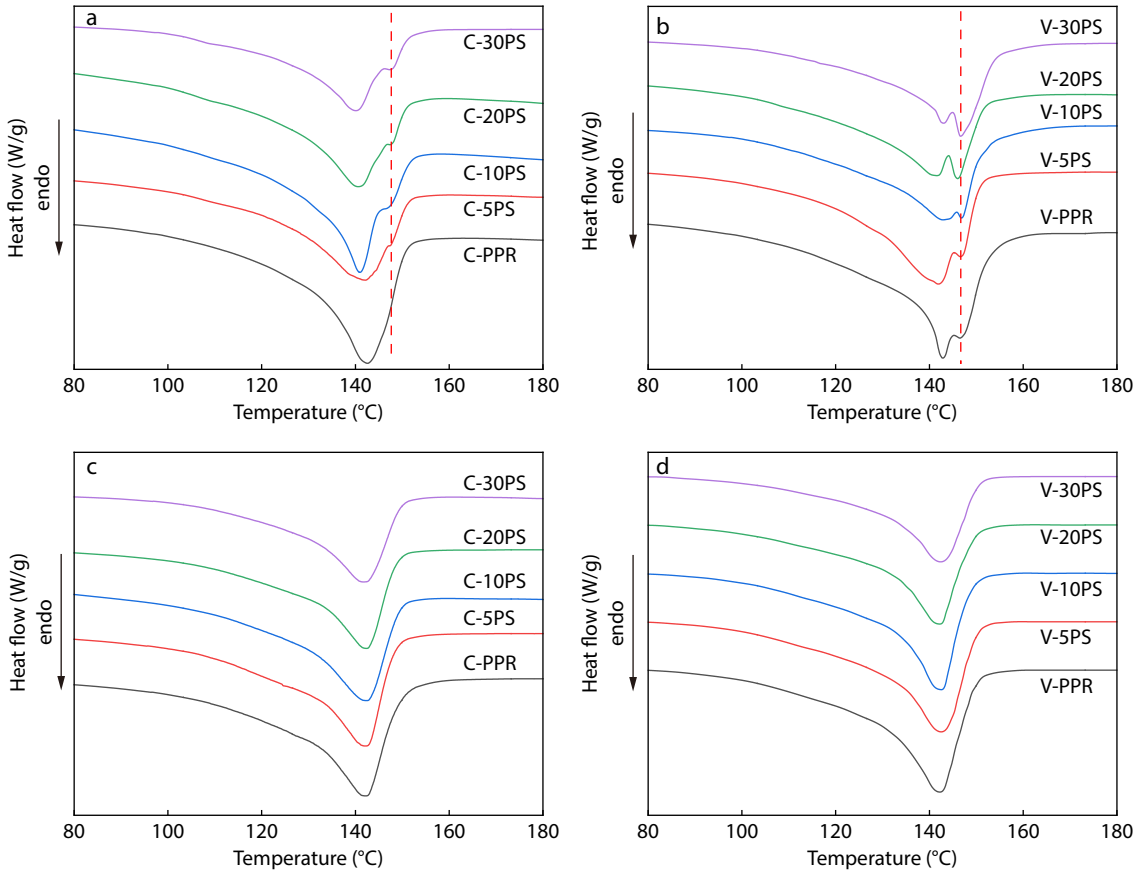

Fig. 5 The 1st melting curves of (a) CIM samples and (b) MFVIM samples; The 2nd melting curves of (c) CIM samples and (d) MFVIM samples.

PPR/PS blends. For CIM samples, we can see that pure PPR has only one melting peak at about 142 °C and the blend containing PS phase exhibits a small shoulder peak at about 146 °C. As the PS phase content increases, the shoulder peak becomes a little more obvious. The melting peak at lower temperature refers to the ordinary spherulites of PPR, and the appearance of shoulder peak represents a highly oriented crystal structure, which is believed to have a higher melt point than the ordinary spherulites.[48] Therefore, due to the weak shear action on CIM samples, there are few oriented crystalls formed in PPR matrix and the addition of PS is beneficial for the formation and maintenance of oriented crystalline structures. For MFVIM samples, the shoulder peak becomes more obvious. When the PS content reaches 20%, the intensity of the shoulder peak is stronger than the peak at lower temperature, which indicates that plenty of oriented crystal structures are formed in PPR due to the strong shear action during MFVIM processing. Compared with CIM samples, MFVIM samples that have undergone multiple melt flow are more conducive to forming oriented structures with higher melting point.

The second melting curves of CIM and MFVIM samples are respectively shown in Figs. 5(c) and 5(d). After eliminating the

https://doi.org/10.1007/s10118-024-3119-3

thermal and mechanical history, all samples have no shoulder peaks after non-isothermal crystallization, which further indicates that the appearance of shoulder peak is caused by external field during the processing process. Table 2 shows the crystallinity calculated from the DSC melting curves. For CIM samples, the crystallinity of pure PPR is 32.6%. After adding PS phase, the crystallinity of the blend slightly increases because of its heterogeneous nucleation effect. Due to the introduction of the strong shear field, the crystallinity of all MFVIM samples exceeds 35%. This is because the shear effect promotes the orientation and physical disentanglement of molecular chains, which is more propitious to the folding and crystallization process,[49,50] ultimately resulting in higher crystallinity than CIM samples. Besides, the crystallinity of all samples obtained from the second melting curves is about 31.5% and remains almost unchanged, indicating that only adding PS phase does not affect the crystallinity of PPR.

In order to futher analyze the kinetics of isothermal crystallization of the blend system after the addition of PS phase, the following avrami equation is used to describe this process:[51,52]

$$1 - X_t = \exp(-Zt^n) \quad (4)$$

where X_t characterizes the relative crystallinity with time, as illustrated in Fig. 6(a), Z is the crystallization rate constant, and n is the Avrami index.

Taking the logarithm on both sides of Eq. (4), we can obtain the following equation:

$$\ln[-\ln(1 - X_t)] = n\ln t + \ln Z \quad (5)$$

Therefore, the values of the slope n and the intercept $\ln Z$ can be obtained by plotting the line of $\ln[-\ln(1 - X_t)]$ against $\ln t$, as shown in Fig. 6(b). When X_t is equal to 0.5, the value of the half-time ($t_{1/2}$) can be calculated, which can be used to estimate the overall rate of isothermal crystallization. The relevant parameters fitted from the Avrami equation are shown in Table 3. From the results, we can see the R^2 of all samples are 0.99, indicating that $\ln[-\ln(1 - X_t)]$ shows a good linear relationship with $\ln t$. Compared to neat PPR, PPR/PS blend ex-

Table 2 DSC results of neat PPR and PPR/PS samples.

	Samples	Melting point (°C)	Fusion enthalpy ΔH_m (J/g)	Crystallinity (%)
1st Melting	C-PPR	142.6	67.46	32.6
	C-5PS	142.2, 146.5	65.09	33.1
	C-10PS	142.3, 146.7	63.14	33.3
	C-20PS	142.1, 146.8	57.51	32.9
	C-30PS	141.9, 146.8	51.02	33.2
	V-PPR	142.1, 146.5	72.81	35.2
	V-5PS	142.1, 146.8	69.08	35.2
	V-10PS	142.8, 146.8	65.46	35.1
	V-20PS	142.4, 146.1	58.62	35.4
	V-30PS	143.0, 146.6	51.29	35.4
2nd Melting	C-PPR	142.1	65.29	31.5
	C-5PS	141.9	62.59	31.8
	C-10PS	142.3	58.65	31.5
	C-20PS	142.1	52.51	31.7
	C-30PS	142.5	45.58	31.5
	V-PPR	142.2	65.17	31.5
	V-5PS	142.3	61.98	31.5
	V-10PS	142.3	58.97	31.7
	V-20PS	142.4	52.32	31.6
	V-30PS	142.5	45.73	31.6

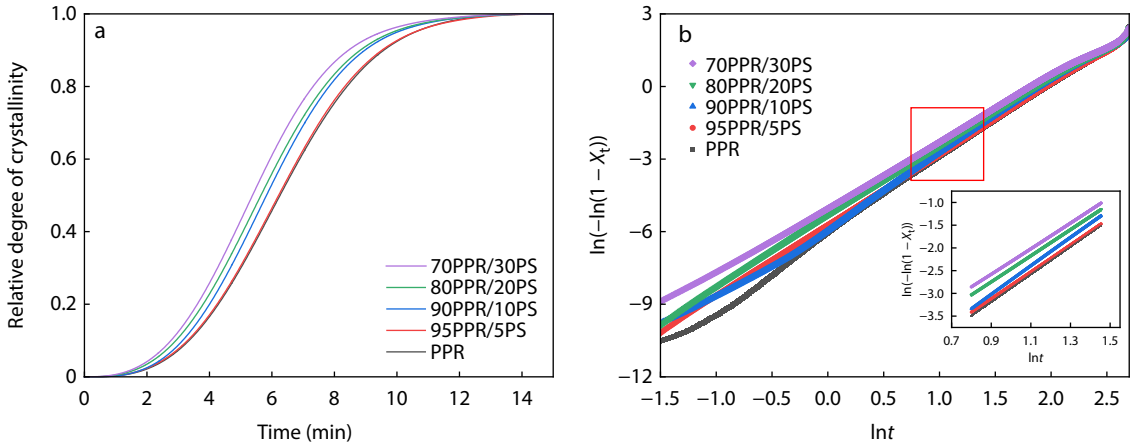

Fig. 6 Isothermal crystallization curves of samples with different PS contents.

https://doi.org/10.1007/s10118-024-3119-3

Table 3 Isothermal crystallization kinetic parameters.

Sample name	n	Z	$t_{1/2}$ (min)	R^2
PPR	3.04	2.68×10^{-3}	6.22	0.99
95PPR/5PS	2.96	2.95×10^{-3}	6.22	0.99
90PPR/10PS	3.12	3.07×10^{-3}	5.75	0.99
80PPR/20PS	2.87	4.82×10^{-3}	5.64	0.99
70PPR/30PS	2.82	5.99×10^{-3}	5.39	0.99

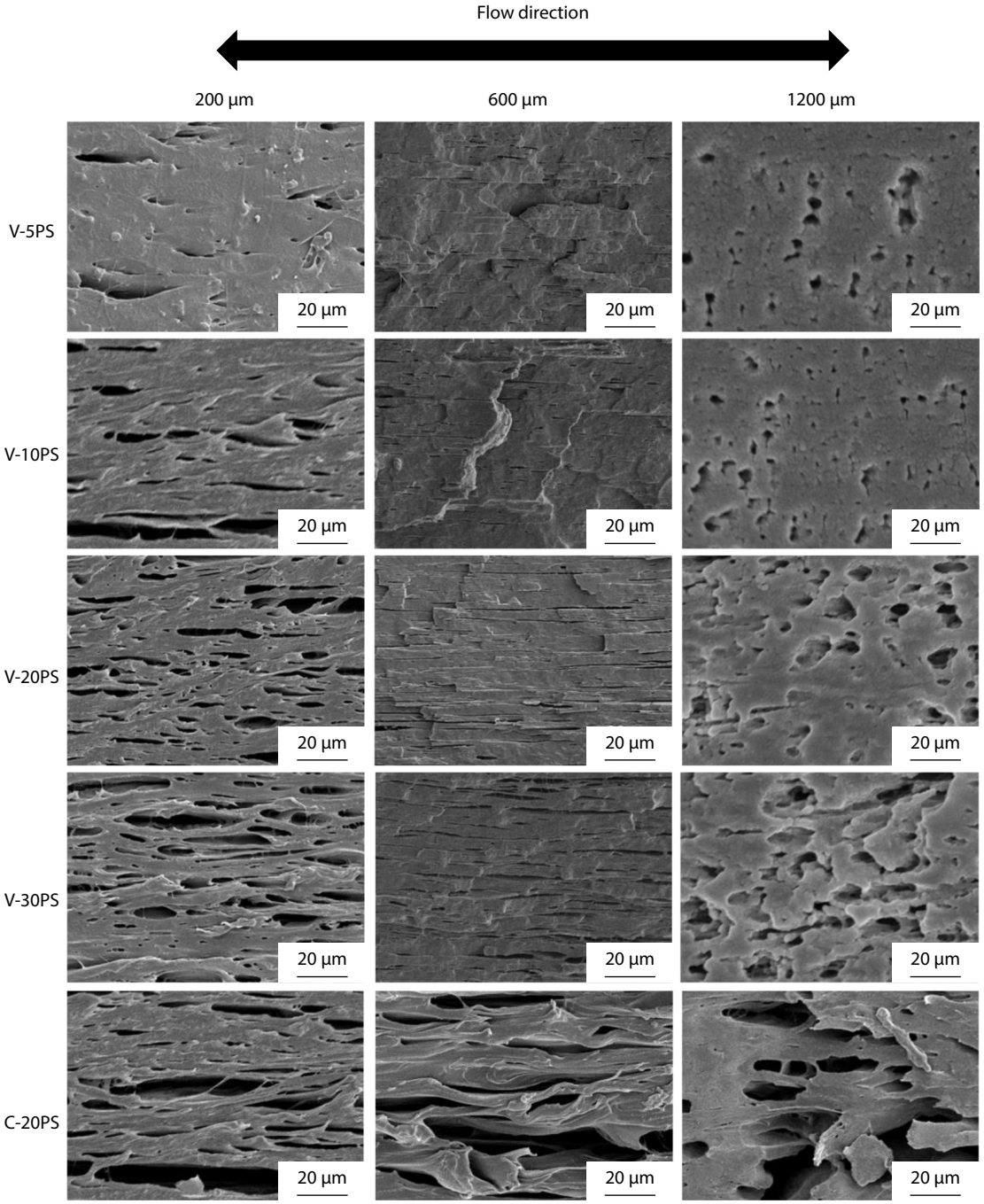

Fig. 7 SEM images of fractured surfaces of different samples at position 1, position 2 and position 3.

hibits faster crystallization rate and it increases with the increase of PS phase content, which is more intuitively manifested as an increase in the crystallization rate constant Z. When the PS content reaches 30%, the value of Z reaches the maximum of 5.99×10^{-3}. $t_{1/2}$ shows a gradually decreasing trend as the increase of PS content, which is reduced from

https://doi.org/10.1007/s10118-024-3119-3

6.22 min of pure PPR sample to 5.39 min of 70PPR/30PS sample. These results all indicate that adding PS phase can promote the crystallization behavior of PPR. In addition, the Avrami index *n* for all samples is close to 3. It indicates that the pure PPR and PPR/PS systems have the same crystallization mechanism, which is a two-dimensional growth process of homogeneous nucleation.[53]

Phase Morphology and Crystal Structure

To investigate the morphology of the dispersed phase, Fig. 7 shows the SEM images of the etched surfaces of the relevant PPR/PS samples. Three representative positions are selected, whose distances from the upper surface are 200, 600 and 1200 μm, and are named as position 1, position 2 position 3, respectively. During the MFVIM molding process, the first flow caused by filling is the same as the CIM process, and the melt undergoes a weak shear effect near the mold wall. Therefore, the PS phase of all samples at position 1 undergoes shear deformation along the direction of melt flow, presenting an irregular elongated shape. For C-20PS sample, PS phase shows rod-shaped structure at position 2 and shows ellipsoid shape at position 3. For MFVIM samples at position 2, the PS phase undergoes strong shear effects caused by multiple melt flow, exhibiting a fibrous distribution in the flow direction. As the PS content increases, the length and diameter of PS microfibers also increase, which is mainly due to two reasons. On the one hand, the viscous force under shear causes dispersed phase particles to elongate along the flow direction, resulting in an increase in specific surface area and surface energy. On the other hand, under the action of interfacial tension, the dispersed phase tends to aggregate and fuse, resulting in a decrease in specific surface area. Thus, the dispersed phase morphology at position 2 is ultimately formed under the joint action of the two reasons. However, the regularity of the formed PS microfibers decreases when the PS phase content reaches 30 wt%. At position 3, the PS phase of all samples is almost unaffected by shear, resulting in an irregular spherical particle dispersion morphology. When the PS content is less than 30%, the samples are inclined to form sea-island structure. Nevertheless, when the PS content reaches 30%, the sample tends to form co-continuous stucture. In order to better evaluate the quality of microfibers, Table 4 provides statistical data on the morphology of PS microfibers at position 2, with an average of 100 microfibers taken from each MFVIM sample. It is found that the length of PS microfibers increases from 18.2 μm to 64.4 μm and the diameter increases from 0.56 μm to 1.12 μm with the increase of PS phase content, indicating that interfacial tension causes PS phase to aggregate first and then deform into microfibers under shear, resulting in larger length and diameter of microfibers in samples with higher PS content. From the results, the aspect ratio of V-20PS sample is the highest, which means the quality of its microfibers is the best.

Table 4 Statistics results about PS phase in shear region.

Sample name	Average length (μm)	Average diameter (μm)	Average aspect ratio
V-5PS	18.2	0.56	32.5
V-10PS	23.4	0.64	36.6
V-20PS	58.6	0.87	67.4
V-30PS	64.4	1.12	57.5

In addition to the phase morphology, crystal structure also has an important impact on material properties.[54,55] In order to obtain more detailed information on the crystal structure at position 2, the amorphous region was etched using a mixed acid solution. Taking V-PPR and V-20PS as examples, the results are shown in Fig. 8. We can see that the typical shish-kebab oriented structures are formed both in V-PPR sample and V-20PS sample. However, for V-PPR sample, the density and quantity of shish-kebab are both lower, and the size is also relatively smaller. Meanwhile, in V-20PS sample we can find lots of hybrid shish-kebab structures, which means the kebabs are epitaxially grown on the PS microfibers. Fig. 9 shows a schematic diagram of the microstructure formation after exerting a strong shear field. The first image shows the blends in the melt state, in which the PPR molecular chains are in a random state and the PS is randomly distributed in the PPR matrix in ellipsoidal shape. The second image exhibits the melt state of the blend after introducing a strong shear field. The PPR molecular chains are highly oriented along the shear direction and many microfibers are formed for the PS phase. The third image shows the crystal structure formed during the cooling crystallization. The PPR molecular chains are regularly oriented and arranged by the shear action, forming a typical shish-kebab crystal structure. Simultaneously, if the PPR molecular chains are close to the surface of the PS phase, they will be adsorbed by microfibers, forming a hybrid shish-kebab structure.

In order to further illustrate the characteristics of crystal structure and the existence of orientation structure in the MFVIM samples, Fig. 10 shows the 2D-SAXS scattering patterns of each sample at position 1, position 2 and position 3. It can be seen that at position 1 and position 2, all the samples exhibit scattering images similar to light bulbs along the

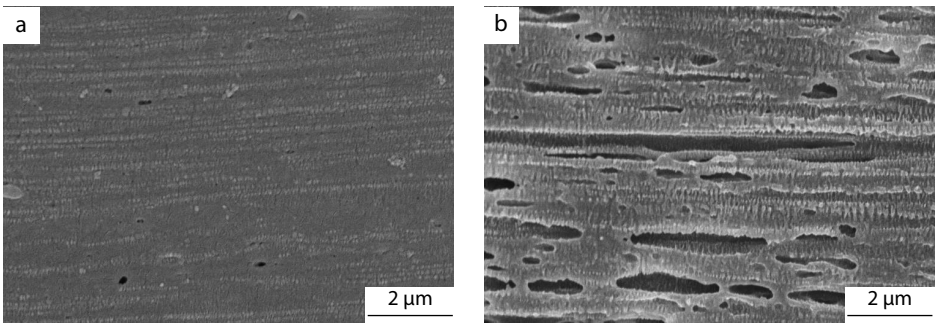

Fig. 8 The crystalline structure for (a) V-PPR, (b) V-20PS.

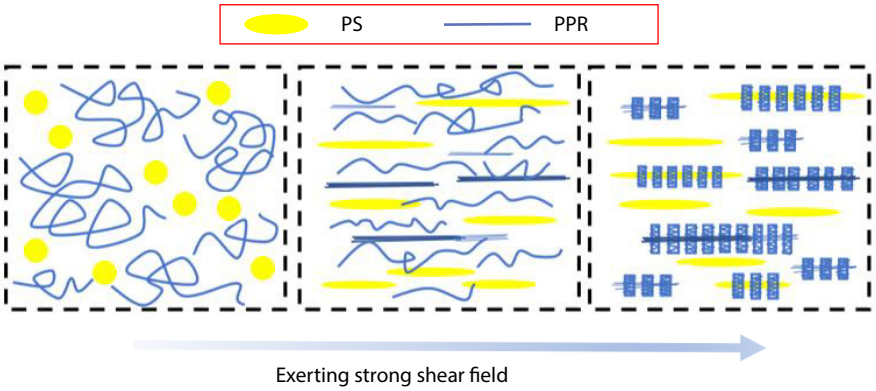

Fig. 9 Schematic diagram for the PPR/PS blend after exerting a strong shear field.

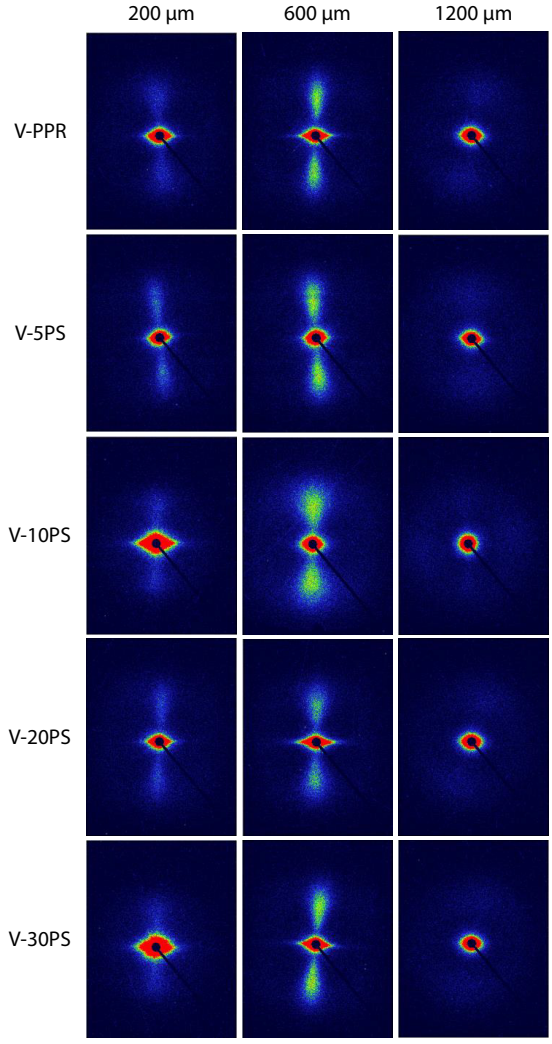

Fig. 10 2D-SAXS patterns of neat PPR and PPR/PS MFVIM samples at position 1, position 2 and position 3.

meridian direction, which is the signals from the kebab structure. While the orientation signals along the equatorial direction represents the existence of shish structure. These phenomena indicate that the typical shish-kebab structure is formed in MFVIM samples. Few shish-kebab structures are formed at position 1 during the filling stage, and most of the rest are formed at position 2 during the vibration process. Therefore, the scattering intensity of the samples at position 2 is much stronger than that at position 1, indicating that applying a strong flow shear field through MFVIM can fully straighten the PPR molecular chain and align it in the direction of melt flow, and finally forming a crystal structure with higher orientation. Besides, there is no obvious orientation signals at position 3 of the samples, which means the melt here are not affected by shear action.

Long period (L_p) represents the repetition distance between the crystalline and amorphous regions, which is of great significance for the study of crystal morphology.[56] Fig. 11 shows the 1D-SAXS curve of the samples at position 2. Based on the Bragg equation ($L = 2\pi/q_{max}$), combined with DSC and SAXS results, the long period (L_p) and crystal thickness (L_c) were calculated, and the results are shown in Table 5. It is shown that the L_p of the samples increases with the increase of PS phase content, from 19.51 nm of the V-PPR sam-

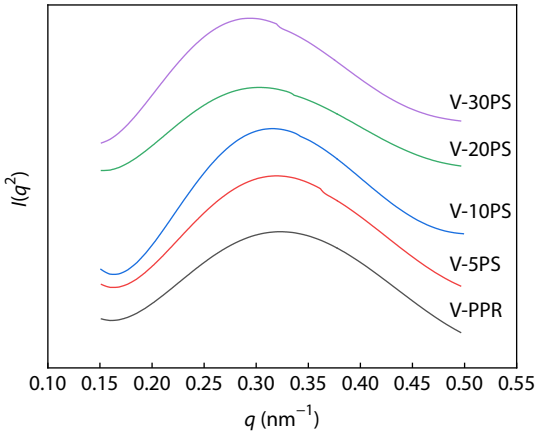

Fig. 11 1D-SAXS intensity profiles of neat PPR and PPR/PS samples at shear region.

Table 5 The q, L_p and L_c values of different samples.

Sample	q (nm^{-1})	L_p (nm)	L_c (nm)
V-PPR	0.322	19.51	6.87
V-5PS	0.319	19.69	6.93
V-10PS	0.316	19.88	6.98
V-20PS	0.302	20.81	7.37
V-30PS	0.294	21.37	7.56

https://doi.org/10.1007/s10118-024-3119-3

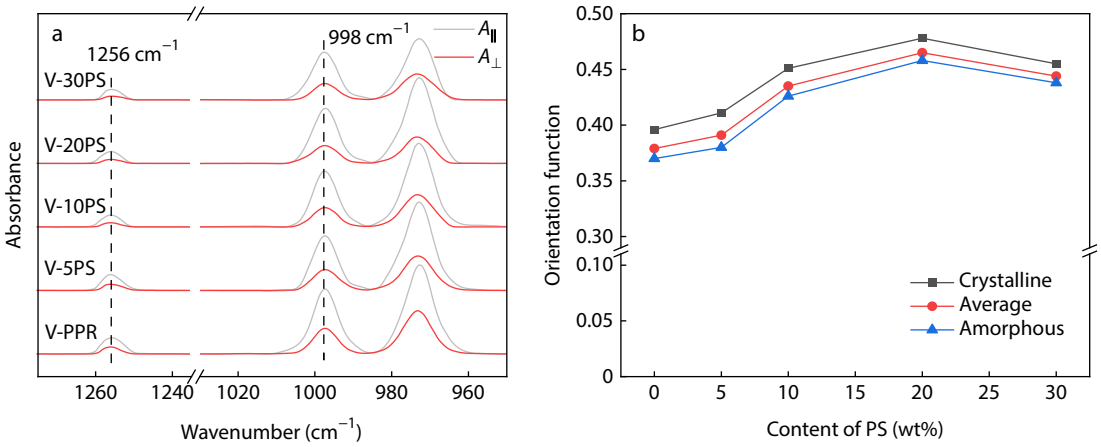

Fig. 12 (a) Polarized FTIR spectra of MFVIM samples; (b) Orientation functions of PPR crystalline, amorphous phase and average situation as a function of PS content.

ple to 21.37 nm of the V-30PS sample, and the corresponding Lc increases from 6.87 nm to 7.56 nm. This is because a lot of shish-kebab and hybrid shish-kebab structures are formed as we discussed above.

Orientation Degree

In the polarization infrared spectra (Fig. 12), the band at 998 cm^{-1} attributes to the crystal region of PP,[57] which can be used to calculate the orientation degree. The band at 1153 cm^{-1} attributes to the amorphous region of PP, but this band overlaps with the absorption band related to the crystal region at 1165 cm^{-1}.[57] Therefore, it is not suitable for calculating the orientation degree of the amorphous region. Meanwhile, the band at 1256 cm^{-1} is related to both the crystalline and amorphous regions of PP,[58] which can be used to calculate the average orientation degree of PP. Due to the inability to directly calculate the orientation degree of the amorphous region of PP, a two-phase model can be used for roundabout calculation:[59]

$$f_{av} = X_c f_c + (1 - X_c) f_a \quad (6)$$

where f_{av} is the average degree of orientation, X_c is the crystallinity, f_c is the orientation degree of the cystal region, f_a is the orientation degree of the amorphous region.

Fig. 12 shows the polarization infrared spectroscopy and orientation calculation results of the characteristic peak area of the MFVIM sample at position 2. Overall, the orientation degree of the crystal region of the samples is higher than that of the amorphous region. Meanwhile, the orientation degree of PPR/PS samples is higher than that of neat PPR samples, indicating that adding PS phase is beneficial for the orientation of PPR molecular chains under the shear effect caused by multiple melt flow. When the PS phase content is below 20 wt%, the orientation degree of PPR increases with the increase of PS content. However, when the PS phase content reaches 30 wt%, the orientation degree decreases. This is due to the decreased regularity of *in situ* microfibers. The blend tends to form co-continuous structure when the PS content is up to 30 wt%, which is no longer conducive to the orientation of the PPR matrix.

Mechanical Properties

Fig. 13 shows the tensile properties of all samples. For CIM samples, the compatibility between PPR and PS is poor, so the tensile strength decreases with the increase of PS phase content. Meanwhile, the Young's modulus increases slightly, which is caused by the much higher modulus of dispersed phase PS than that of matrix phase PPR. For MFVIM samples, due to the introduction of multiple melt flow shear fields, the tensile strength increases with the increase of PS content when the PS content is below 20%. This trend is different from that of CIM samples, which is because not only PS *in situ* microfibers but also oriented shish-kebab and hybrid shish-kebab stuctures in the MFVIM sample can jointly improve the mechanical properties of materials. When the PS phase content is 20 wt%, the tensile strength and Young's modulus of MFVIM sample reach 42.4 and 645.6 MPa, which are 125% and 32% higher than those of C-20PS sample, respectively. However, when the PS content increases to 30 wt%, there is no significant change in tensile strength. But the Young's modulus continuously increases to 730.8 MPa with the increase of PS content.

Fig. 14 shows the notch impact strength of all samples. For pure PPR, the impact resistance is already good, and the shear effect can only slightly improve the impact strength. Whether it is CIM or MFVIM sample, the impact strength decreases with the increase of PS content, which is inevitably caused by the incompatibility between PPR and PS. Moreover, the impact strength of CIM samples shows a sharp downward trend as the increase of PS phase, but the impact strength of MFVIM samples only slightly decreases within the PS content range of 5% to 20%. Therefore, for samples with the same PS phase content, the impact strength of MFVIM samples is markedly improved compared to CIM samples. When the PS content is 5%, the impact strength of MFVIM sample is twice that of CIM sample. When the PS phase content is 20 wt%, the impact strength increases from 6.3 kJ/m^2 of CIM sample to 25.8 kJ/m^2 of MFVIM sample with an increase of approximately 310%. The reason is that the V-20PS sample has the best quality of the PS *in situ* microfibers and contains plenty of shish-kebab stuctures, which makes it relatively superior mechanical properties. However, when the PS phase reaches up to 30 wt%, the decrease of the impact strength of MFVIM samples is particularly obvious, which is owning to the reduced microfiber regularity. Therefore, by adjusting the PS phase content reasonably and adopting suitable molding methods, the de-

https://doi.org/10.1007/s10118-024-3119-3

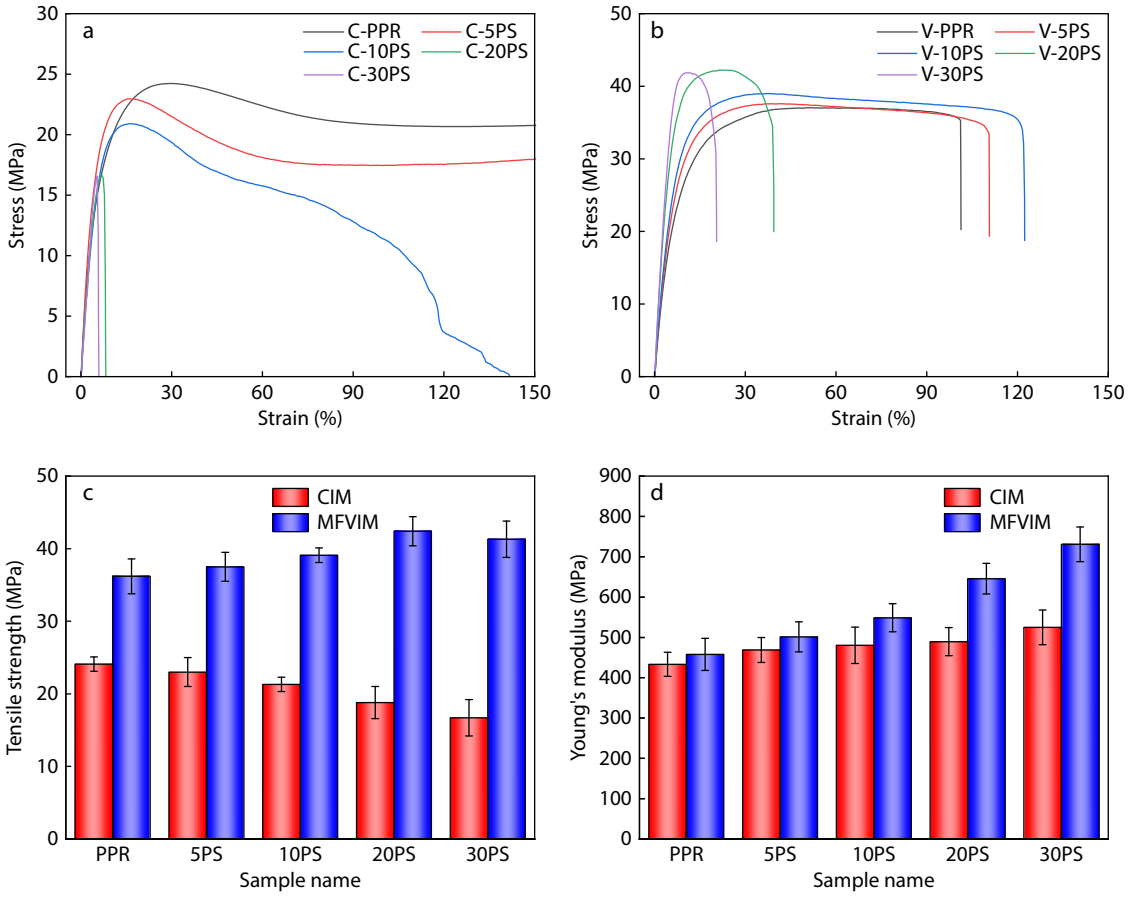

Fig. 13 The tensile properties of different samples: (a, b) typical stress-strain curves, (c, d) tensile strength and Young's modulus.

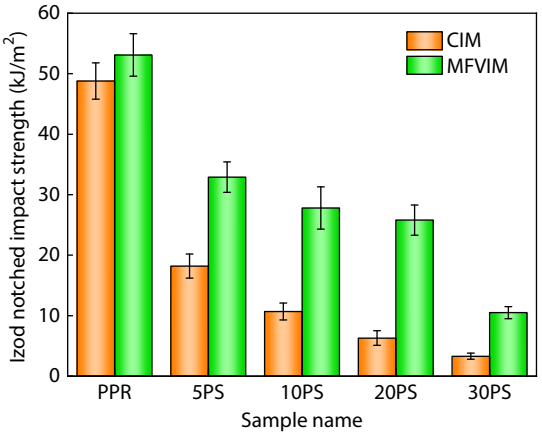

Fig. 14 The impact strength of different samples.

crease of the impact performance can be controlled. Based on the comprehensive testing results of the mechanical properties, it can be concluded that the MFVIM sample with a PS phase content of 20 wt% has relatively high tensile strength and impact strength, indicating that a PPR strength-toughness balanced material can be successfully prepared.

CONCLUSIONS

In this work, we successfully prepared MFCs of PPR/PS blend with different blending ratios using MFVIM technology. On the one hand, the PS phase is fully deformed into microfibers due to the strong shear effect, and the length, diameter and aspect ratio of the microfibers change with the change of the PS phase content. On the other hand, PPR can form shish-kebab structures under the action of shear and can be absorbed by PS microfibers to form hybrid shish-kebab structures. When the PS content is 20%, the morphology and quality of the microfibers are optimal, and a large number of shish-kebab and hybrid shish-kebab structures are observed. Under the joint action of these two aspects, the mechanical properties of the samples are also greatly improved. Therefore, a strong and tough balanced PPR based material is obtained, which provides a new approach for the wider application of PPR in industry and daily life.

Conflict of Interests

The authors declare no interest conflict.

Data Availability Statement

The data that support the findings of this study are available on request from the corresponding author upon reasonable request. The authors' contact information: 1134861446@qq.com; zhangjie@scu.edu.cn.

https://doi.org/10.1007/s10118-024-3119-3

ACKNOWLEDGMENTS

This work was financially supported by the National Natural Science Foundation of China (No.21627804).

REFERENCES

1 Ma, T. B.; Ma, H.; Ruan, K. P.; Shi, X. T.; Qiu, H.; Gao, S. Y.; Gu, J. W. Thermally conductive poly(lactic acid) composites with superior electromagnetic shielding performances *via* 3D printing technology. *Chinese J. Polym. Sci.* **2022**, *40*, 248–255.
2 Wang, K.; Chen, F.; Li, Z. M.; Fu, Q. Control of the hierarchical structure of polymer articles *via* "structuring" processing. *Prog. Polym. Sci.* **2014**, *39*, 891–920.
3 Zhou, M.; Li, X. P.; Jin, M.; Xia, C.; Shen, K. Z.; Zhang, J. Simultaneously improving the tensile and impact properties of isotactic polypropylene with the cooperation of co-PP and *β*-nucleating agent through pressure vibration injection molding. *Chinese J. Polym. Sci.* **2016**, *34*, 1001–1013.
4 Kalay, G.; Bevis, M. J. Processing and physical property relationships in injection-molded isotactic polypropylene. 1. Mechanical properties. *J. Polym. Sci., Part B: Polym. Phys.* **1997**, *35*, 241–263.
5 Liang, S.; Wang, K.; Tang, C. Y.; Zhang, Q.; Du, R. N.; Fu, Q. Unexpected molecular weight dependence of shish-kebab structure in the oriented linear low density polyethylene/high density polyethylene blends. *J. Chem. Phys.* **2008**, *128*, 174902.
6 Liu, T.; Huang, A.; Geng, L. H.; Lian, X. H.; Chen, B. Y.; Hsiao, B. S.; Kuang, T. R.; Peng, X. F. Ultra-strong, tough and high wear resistance high-density polyethylene for structural engineering application: a facile strategy towards using the combination of extensional dynamic oscillatory shear flow and ultra-high-molecular-weight polyethylene. *Compos. Sci. Technol.* **2018**, *167*, 301–312.
7 Hong, R.; Jiang, Y. X.; Leng, J.; Liu, M. J.; Shen, K. Z.; Fu, Q.; Zhang, J. Synergic enhancement of high-density polyethylene through ultrahigh molecular weight polyethylene and multi-flow vibration injection molding: a facile fabrication with potential industrial prospects. *Chinese J. Polym. Sci.* **2021**, *39*, 756–769.
8 Mi, D. S.; Xia, C.; Jin, M.; Wang, F. F.; Shen, K. Z.; Zhang, J. Quantification of the effect of shish-Kebab structure on the mechanical properties of polypropylene samples by controlling shear layer thickness. *Macromolecules* **2016**, *49*, 4571–4578.
9 Hou, F. Y.; Mi, D. S.; Zhou, M.; Zhang, J. The influences of a novel shear layer-spherulites layer alternated structure on the mechanical properties of injection-molded isotactic polypropylene. *Polymer* **2017**, *122*, 12–21.
10 Huang, L. X.; Wang, Z.; Zheng, G. Q.; Guo, J. Z. H.; Dai, K.; Liu, C. T. Enhancing oriented crystals in injection-molded HDPE through introduction of pre-shear. *Mater. Desigh.* **2015**, *78*, 12–18.
11 Mi, D. S.; Hou, F. Y.; Zhou, M.; Zhang, J. Improving the mechanical and thermal properties of shish-kebab *via* partial melting and re-crystallization. *Eur. Polym. J.* **2018**, *101*, 1–11.
12 Liu, Q.; Li, H. H.; Yan S. K. Structure and properties of *β*-polypropylene reinforced by polypropylene fiber and polyamide fiber. *Chinese J. Polym. Sci.* **2014**, *32*, 509–518.
13 Ma, L. L.; Liu, F.; Liu, D. Y.; Liu Y. L. Review of strain rate effects of fiber-reinforced polymer composites. *Polymers* **2021**, *13*, 2839.
14 Alarifi, I. M. A review on factors affecting machinability and properties of fiber-reinforced polymer composites. *J. Nat. Fibers* **2023**, *20*, 2154304.
15 Kelnar, I.; Fortelný, I.; Kaprálková, L.; Kratochvíl, J.; Angelov, B.; Nevoralová, M. Effect of layered silicates on fibril formation and properties of PCL/PLA microfibrillar composites. *J. Appl. Polym. Sci.* **2016**, *133*, 43061.
16 Fakirov, S. Nano-/microfibrillar polymer-polymer and single polymer composites: the converting instead of adding concept. *Compos. Sci. Technol.* **2013**, *89*, 211–225.
17 Li, X. G.; Xin, C. L.; Huang, Y.; Kang, K.; He, Y. D. Effect of dispersed phase on the morphology of *in situ* microfibrils and the viscoelastic properties of its composite *via* direct extrusion. *J. Appl. Polym. Sci.* **2018**, *135*, 46286.
18 Raghavan, S. R.; Douglas, J. F. The conundrum of gel formation by molecular nanofibers, wormlike micelles, and filamentous proteins: gelation without cross-links. *Soft Matter* **2012**, *8*, 8539–8546.
19 Wang, J. F.; Zhang, X. L.; Zhao, T. B.; Shen, L. Y.; Wu, H. Guo, S. Y. Morphologies and properties of polycarbonate/polyethylene *in situ* microfibrillar composites prepared through multistage stretching extrusion. *J. Appl. Polym. Sci.* **2014**, *131*, 40108.
20 Rizvi, A.; Tabatabaei, A.; Barzegari, M. R.; Mahmood, S. H.; Park, C. B. *In situ* fibrillation of CO_2-philic polymers: Sustainable route to polymer foams in a continuous process. *Polymer*. **2013**, *54*, 4645-4652.
21 Fakirov, S.; Bhattacharyya, D.; Shields, R. J. Nanofibril reinforced composites from polymer blends. *Colloid Surface A* **2008**, *313*, 2–8.
22 Jiang, Y. X.; Mi, D. S.; Wang, Y. X.; Wang, T.; Shen, K. Z.; Zhang, J. Composite contains large content of in situ microfibril, prepared directly by injection molding: morphology and property. *Macromol. Mater. Eng.* **2018**, *303*, 1800270.
23 Zhou, Y. G.; Su, B.; Wu, H. H. Effect of cold-drawn fibers on the self-reinforcement of PP/LDPE composites. *J. Mater. Eng. Perform.* **2017**, *26*, 4072–4082.
24 Zhou, Y. G.; Su, B.; Turng, L. S. Influence of processing conditions on the morphological structure and ductility of water-foamed injection molded PP/LDPE blended parts. *Cell Polym.* **2017**, *36*, 51–74.
25 Kelnar, I.; Kaprálková, L.; Kratochvíl, J.; Kotek, J.; Kobera, L.; Rotrekl, J. Hromádková, J. Effect of nanofiller on the behavior of a melt-drawn HDPE/PA6 microfibrillar composite. *J. Appl. Polym. Sci.* **2015**, *132*, 41868.
26 Dadouche, T.; Yousfi, M.; Samuel, C.; Lacrampe, M. F.; Soulestin, J. (Nano) Fibrillar morphology development in biobased poly(butylene succinate-*co*-adipate)/poly(amide-11) blown films. *Polym. Eng. Sci.* **2021**, *61*, 1324-1337.
27 Jiang, Y. X.; Wu, J. J.; Leng, J.; Cardon, L.; Zhang, J. Reinforced and toughened PP/PS composites prepared by Fused Filament Fabrication (FFF) with *in-situ* microfibril and shish-kebab structure. *Polymer* **2020**, *186*, 121971.
28 Xia, X. C.; Yang, W.; Zhang, Q. P.; Wang, L.; He, S.; Yang, M. B. Large scale formation of various highly oriented structures in polyethylene/polycarbonate microfibril blends subjected to secondary melt flow. *Polymer* **2014**, *55*, 6399–6408.
29 Jiang, Y. X.; Mi, D. S.; Wang, Y. X.; Wang, T.; Shen, K. Z.; Zhang, J. Insight into understanding the influence of blending ratio on the structure and properties of high-density polyethylene/polystyrene microfibril composites prepared by vibration injection molding. *Ind. Eng. Chem. Res.* **2019**, *58*, 1190–1199.
30 Gu, X. B.; Wang, Y. X.; Jiang, Y. X.; Liu, M. J.; Fu, Q.; Zhang, J. High impact performance induced by a synergistic effect of heteroepitaxy and oriented layer-unoriented layer alternated structure in *i*PP/HDPE injection molded part. *Polymer.* **2019**, *175*, 206–214.
31 He, P.; Xiao, Y.; Zhang, P. M.; Xing, C. H.; Zhu, N.; Zhu, X. Y.; Yan, D. Y. Thermal degradation of syndiotactic polypropylene and the influence of stereoregularity on the thermal degradation behaviour by *in situ* FTIR spectroscopy. *Polym. Degrad. Stabil.* **2005**, *88*, 473–479.
32 Tokiwa, Y.; Calabia, B. P.; Ugwu, C. U.; Aiba, S. Biodegradability of plastics. *Int. J. Mol. Sci.* **2009**, *10*, 3722–3742.
33 Zhang, Q.; Yang, H.; Fu, Q. Kinetics-controlled compatibilization of immiscible polypropylene/polystyrene blends using nano-SiO_2 particles. *Polymer* **2004**, *45*, 1913–1922.
34 Zhang, X. Q.; Zhao, Y.; Wang, Z. G.; Zheng, C. X.; Dong, X.; Su, Z. Q.;

Sun, P.Y.; Wang, D. J.; Han, C. C.; Xu, D. F. Morphology and mechanical behavior of isotactic polypropylene (*i*PP)/syndiotactic polypropylene (*s*PP) blends and fibers. *Polymer* **2005**, *46*, 5956–5965.
35 Li, M.; Li, G.; Fan, Y. F.; Jiang, J.; Ding, Q.; Dai, X.; Mai, K. C. Effect of nano-ZnO-supported 13X zeolite on photo-oxidation degradation and antimicrobial properties of polypropylene random copolymer. *Polym. Bull.* **2014**, *71*, 2981–2997.
36 Li, X.; Pi, L.; Nie, M.; Wang, Q. Joint effects of rotational extrusion and TiO_2 on performance and antimicrobial properties of extruded polypropylene copolymer pipes. *J. Appl. Polym. Sci.* **2015**, *132*, 42410.
37 Cao, J.; Lü, Q. F. Crystalline structure, morphology and mechanical properties of *β*-nucleated controlled-rheology polypropylene random copolymers. *Polym. Test.* **2011**, *30*, 899–906.
38 Luo, F.; Wang, K.; Wang, J. W.; Deng, H.; Zhang, Q.; Chen, F.; Fu, Q.; Na, B. Tailoring toughness of injection molded bar of polypropylene random copolymer through processing melt temperature. *Polym. Int.* **2011**, *60*, 1705–1714.
39 Chen, H. B.; Karger-Kocsis, J.; Wu, J. S.; Varga, J. Fracture toughness of *α*- and *β*-phase polypropylene homopolymers and random-and block-copolymers. *Polymer.* **2002**, *43*, 6505–6514.
40 Maier, C.; Calafut, T. in *Polypropylene: the definitive user's guide and databook*. William Andrew, **1998**.
41 Su, R.; Wang, K.; Zhang, Q.; Chen, F.; Fu, Q. Orientation and epitaxy in the injection-molded bars of linear low-density polyethylene/isotactic polypropylene blends: an infrared dichroism measurement. *J. Phys. Chem. B* **2009**, *113*, 7423–7429.
42 Su, R.; Wang, K.; Ning, N. Y.; Chen, F.; Zhang, Q.; Wang, C. Y.; Fu, Q.; Na, B. Orientation in high-density polyethylene/inorganic whisker composite fibers as studied *via* polarized Fourier transform infrared spectroscopy. *Compos. Sci. Technol.* **2010**, *70*, 685–691.
43 Lu, J. J.; Sue, H. J. Characterization of crystalline texture of LLDPE blown films using X-ray pole figures. *Macromolecules* **2001**, *34*, 2015–2017.
44 Min, K.; White, J. L.; Fellers, J. F. Development of phase morphology in incompatible polymer blends during mixing and its variation in extrusion. *Polym. Eng. Sci.* **1984**, *24*, 1327–1336.
45 Yi, X.; Xu, L.; Wang, Y. L.; Zhong, G. J.; Ji, X.; Li, Z. M. Morphology and properties of isotactic polypropylene/poly(ethylene terephthalate) in situ microfibrillar reinforced blends: influence of viscosity ratio. *Eur. Polym. J.* **2010**, *46*, 719–730.
46 Heino, M. T.; Hietaojia, P. T.; Vainio, T. P.; Seppälä, J. V. Effect of viscosity ratio and processing conditions on the morphology of blends of liquid crystalline polymer and polypropylene. *J. Appl. Polym. Sci.* **1994**, *51*, 259–270.
47 Li, Z.; Sun, C. X.; Li, X. Y.; Zhang, Q.; Fu, Q. In situ formation of polypropylene (PP) fibrils in the olefinic block copolymer (OBC): effect of viscosity ratio and OBC block architecture. *RSC Adv.* **2015**, *5*, 85442–85445.
48 Qi, Y. X.; Zhang, C. B.; Zhao, Y.; Wang, D. J.; Lei, J.; Li, Z. M. Synergistic enhancement of crystallization and mechanical performance of polypropylene random copolymer by strong shear and *β*-nucleating agent. *Polym. Int.* **2017**, *66*, 1141–1150.
49 Hu, J. W.; Chen, J.; Yang, T.; Wang, P. B.; Min, J.; Fu, Q.; Zhang, J. Regulation of entanglement networks under different shear fields and its effect on the properties of poly(l-lactide). *Ind. Eng. Chem. Res.* **2023**, *62*, 7434–7446.
50 Mi, D. S.; La, R. X.; Wang, T.; Zhang, X. W.; Zhang, J. Hierarchic structure and mechanical property of glass fiber reinforced isotactic polypropylene composites molded by multiflow vibration injection molding. *Polym. Compo.* **2017**, *38*, 2707–2717.
51 Tomka, J. Note on the use of the Avrami equation for the interpretation of the primary crystallization of polymers. *Eur. Polym. J.* **1968**, *4*, 237–240.
52 Khonakdar, H. A.; Shiri, M.; Golriz, M.; Asadinezhad, A.; Jafari, S. H. A novel analytical approach to estimate isothermal and dynamic crystallization Avrami kinetic parameters. *e-Polymers* **2008**, *8*, 085.
53 Yang, J.; McCoy, B. J.; Madras, G. Distribution kinetics of polymer crystallization and the Avrami equation. *J. Chem. Phys.* **2005**, *122*, 064901.
54 Mi, D. S.; Wang, Y. X.; Kuzmanovic, M.; Delva, L.; Jiang, Y. X.; Cardon, L.; Zhang, J.; Ragaert, K. Effects of phase morphology on mechanical properties: oriented/unoriented PP crystal combination with spherical/microfibrillar PET phase. *Polymers* **2019**, *11*, 248.
55 Hu, M. L.; Deng, C. J.; Gu, X. B.; Fu, Q.; Zhang, J. Manipulating the strength-toughness balance of poly(l-lactide) (PLLA) *via* introducing ductile poly(*ε*-caprolactone) (PCL) and strong shear flow. *Ind. Eng. Chem. Res.* **2019**, *59*, 1000–1009.
56 Zhang, Y. W.; Chen, J.; Fu, Q.; Zhang, J. Novel strategy to improve the performance of poly(l-lactide): the synergistic effect of disentanglement and strong shear field. *ACS Sustainable Chem. Eng.* **2023**, *11*, 9630–9642.
57 Painter, P. C.; Watzek, M.; Koenig, J. L. Fourier transform infra-red study of polypropylene. *Polymer* **1977**, *18*, 1169–1172.
58 Zhang, Y.; Xin, C. L.; Su, Y. B.; He, Y. D. The effect of unidirectional shear flow-induced orientation on foaming properties of polypropylene. *J. Polym. Eng.* **2020**, *40*, 193–202.
59 Siesler, H. W. Rheo-optical Fourier-transform infrared spectroscopy: vibrational spectra and mechanical properties of polymers. *Adv. Polym. Sci.* **2005**, *65*, 1–77.

https://doi.org/10.1007/s10118-024-3119-3